# Optical Isolation based on Space-time Engineered Asymmetric Photonic Bandgaps

Nima Chamanara, Sajjad Taravati, Zoé-Lise Deck-Léger, and Christophe Caloz
*Poly-Grames Research Center,*
*École Polytechnique de Montréal,*
*Montréal, Québec H3T 1J4, Canada.*
(Dated: December 28, 2016)

Nonreciprocal electromagnetic devices play an important role in modern optical and microwave technologies. Conventional methods for realizing such systems are incompatible with integrated circuits. With recent advances in integrated photonics, the need for efficient on-chip magnetless nonreciprocal devices is more urgent than ever. This paper leverages space-time engineered asymmetric photonic bandgaps to generate optical isolation. It is shown that a properly designed space-time modulated slab is highly reflective/transparent for opposite directions of propagation. The proposed method requires a low modulation frequency, is magnetless and can achieve very high isolation levels. Experimental proof of concept at microwave frequencies is provided.

arXiv:1612.08398v1 [physics.optics] 26 Dec 2016

## I. INTRODUCTION

Electromagnetic nonreciprocity plays a crucial role in modern electronic and optical technologies. Historically, breaking Lorentz reciprocity relies on magnetically biased magnetoelectric [1, 2] and magnetoplasmonic [3–7] materials. However, magnetic materials are incompatible with integrated circuit technology. Moreover, such magnet-based techniques rely on bulky expensive magnets which are undesirable in compact integrated systems. With the emergence of integrated photonics [8–11], genering on-chip optical nonreciprocity is of paramount importance.

Extensive efforts have been devoted during the last decades to produce magnetless nonreciprocity, to eliminate the undesirable magnet and magnetic materials. Unilateral components such as transistors break Lorentz reciprocity, and have been used for over 50 years in microwave nonreciprocal components and more recently in nonreciprocal metamaterials. Nonreciprocal transistor-based circulators [12–15], nonreciprocal metamaterials based on unidirectional transistor-based unit cells [16–20], and nonreciprocal components based on staggered switched delay lines [21] belong to this category. Although these methods are compatible with integrated circuit technology, they have limited power and noise performance [22]. Moreover, their application at optical frequencies is impeded by frequency limitations of transistor technology.

The Lorentz reciprocity theorem does not apply to nonlinear materials. This fact has spurred many efforts to break Lorentz reciprocity in nonlinear media, and produce magnetless nonlinear-based nonreciprocity [23–28]. In this approach the asymmetry in the electromagnetic field intensity profile of an asymmetric permittivity profile is leveraged for producing nonreciprocity. If nonlinearity is introduced at locations where the forward and backward waves have a significant difference in their electromagnetic field intensity, the forward and backward waves would see different permittivity landscapes and the structure exhibits nonreciprocity. However, since nonlinear effects only get pronounced at high signal levels, these techniques exhibit nonreciprocity only over a certain signal power range. it was shown that in the presence of high level input signals in a nonlinear optical isolator, some low level signals would pass through such devices reciprocally, and the structure would not properly function as a nonreciprocal optical component [29].

Balanced loss-gain media, also known as PT-symmetric media [30–32], have been reported to produce unidirectional properties [33–37]. However, the reported nonreciprocal PT-symmetric devices [32, 34], always involve nonlinearity or other reciprocity breaking elements such as magnetic fields and time varying media. Pure loss-gain media, is constrained to be reciprocal according to Lorentz reciprocity theorem and can not produce optical isolation [38, 39].

Space-time modulation is another technique that breaks Lorentz reciprocity [40–44]. Such techniques are well suited for producing nonreciprocity at optical frequencies. There has been several proposals for leveraging space-time variation for achieving magnetless nonreciprocity. The technique proposed by [40] uses oblique space-time interband transitions, between two different modes of an optical waveguide. However, to generate efficient coupling between the two waveguide modes, which are generally orthogonal, this technique requires complex asymmetric modulation schemes. The techniques proposed in [41, 42] is based on counter rotating resonant modes with slightly shifted resonance frequencies. However, although it can achieve nonreciprocity over a subwavelength footprint, this technique requires sophisticated synchronized optical sources [41, 42].

This paper introduces a new concept for realizing optical isolation, based on space-time engineered asymmetric photonic bandgaps. Space-time variation in the permittivity of a medium is used to generate photonic band structures that are asymmetrically aligned with respect to opposite directions of propagation. It is shown that with proper excitation, such a system can operate as a unidirectional optical device. The modulation scheme is uniform across the cross section of the waveguide as op-

posed to [40], and does not require complex transverse nonuniform profiles. The required modulation frequency for generating such nonreciprocity is relatively low, and may be produced with acoustic waves. The proposed structure may find applications in integrated magnetless unidirectional optical systems. An experimental proof of concept at microwave frequencies is presented.

## II. PRINCIPLE OF OPERATION

Consider a reciprocal photonic or microwave bandgap structure, such as a conventional Bragg grating reflector based on spatially periodic variations in the refractive index of a background material such as a single mode optical fiber, or a waveguide with a cut-off. The dispersion curve corresponding to such an structure with a complete bandgap is shown in Fig. 1(a). As the structure is composed of reciprocal materials, the bandgaps are aligned horizontally, i.e. symmetric with respect to positive and negative Bloch-Floquet wavenumbers.

At frequencies corresponding to the bandgap, the Bloch-Floquet modes acquire an imaginary wavenumber and become evanescent. When such an structure is excited at the gap frequencies, the incident wave excites the evanescent gap mode. This mode, marked by the red dot in Fig. 1(a), decays exponentially inside the periodic structure and fades out quickly before reaching the other end of the structure. Therefore with a proper choice of the structure's length, almost no power is transferred to the other side and as a result of energy conservation almost all of the incident power is reflected. Since the dispersion curves are symmetric with respect to opposite directions of propagation, when the structure is excited from the opposite end, similarly the symmetric evanescent Bloch-Floquet mode marked by the blue dot in Fig. 1(a) is excited, and essentially all the power is reflected.

Next consider a structure with oblique asymmetric bandgaps, where the bandgaps are slightly misaligned for positive and negative directions as shown in Fig. 1(b). When such a structure is excited from the left at the frequency corresponding to the horizontal line in Fig. 1(b), the evanescent mode, marked by the red dot, is excited. For a long enough structure almost no power is reached to the opposite end and the wave is fully reflected. However, when the structure is excited from the opposite direction the mode marked by the blue dot in Fig. 1(b), i.e. a propagating mode is excited. Therefore the incident electromagnetic power is transferred to the other side of the structure, and with proper matching it is fully transmitted.

Producing such asymmetric dispersion curves requires a mechanism that breaks Lorentz reciprocity. In the next section we show that such asymmetric gaps may be realized using a space-time varying medium. In a space-time varying medium, electromagnetic waves propagating in opposite directions perceive different landscapes

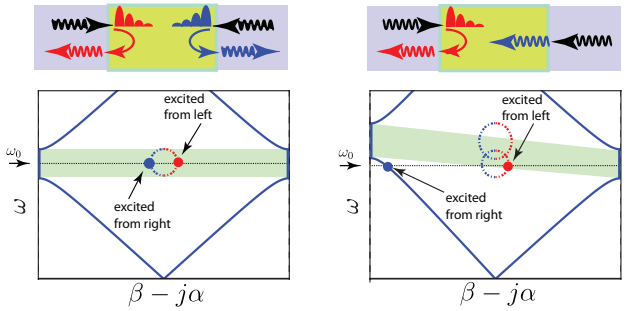


(a) (b)

FIG. 1. Principle of nonreciprocal Bragg reflection based on asymmetric photonic bandgaps. The solid and dashed curves represent the real ($\beta$) and imaginary ($\alpha$) part of the propagation factor, respectively. (a) In a reciprocal periodic system bandgaps are symmetric with respect to positive and negative directions. When the structures is excited from left/right, the evanescent modes marked by red/blue dots are excited, and the incident wave is fully reflected. The horizontal line corresponds to the excitation frequency. (b) The bandgap is tilted with slope $\nu$. When the structure is excited from left/right the modes marked by red/blue dots are excited, which are evanescent/propagating modes. In one direction the wave is totally reflected. In the opposite direction it is fully transmitted. The horizontal line corresponds to the excitation frequency $\omega_0$.

and therefore exhibit nonreciprocity. It is shown that the dispersion curves in such a space-time modulated medium become tilted with slope $\nu$ and hence produce asymmetric bandgaps. A finite space-time modulated slab is then excited at the gap frequency and analyzed.

## III. UNBOUNDED SPACE-TIME MEDIUM

Consider an infinite space-time periodic medium with permittivity

$$\epsilon(\mathbf{r},t) = \epsilon_0\epsilon_r\left[1 + M f_{\text{per}}\left(t \pm z/\nu\right)\right], \tag{1}$$

where $f_{\text{per}}$ is a periodic function with period $T$ and $M$ is the modulation depth. Such a medium represents a periodic Bragg structure whose spatial profile is shifted in time with a velocity $\nu$. Such space-time periodic media were first studied in the context of traveling wave parametric amplification and parametric energy conversion [44–50]. The electric field in such a medium satisfies the following wave equation [48]

$$\nabla^2\mathbf{E} - \mu_0\frac{d^2}{dt^2}\left[\epsilon(\mathbf{r},t)\mathbf{E}\right] = 0. \tag{2}$$

This wave equation admits solutions in the Bloch-Floquet form [48]

$$\mathbf{E} = e^{j(\omega t - \beta z)} \sum_{n=-\infty}^{\infty} \mathbf{E}_n e^{jn(\omega_\mathrm{m} t - k_\mathrm{m} z)}, \tag{3}$$

where $\omega_\mathrm{m} = 2\pi/T$ is the modulation frequency and $k_\mathrm{m} = \omega_\mathrm{m}/\nu$. The dispersion relations for the Bloch-Floquet waves in such a medium is found by substituting (3) in (2). The resulting equation reduces to a matrix equation $\mathbf{Ax} = \mathbf{0}$, through orthogonality of Fourier harmonics. Nullifying the determinant $|\mathbf{A}| = 0$, which is generally done numerically, produces the dispersion curves.

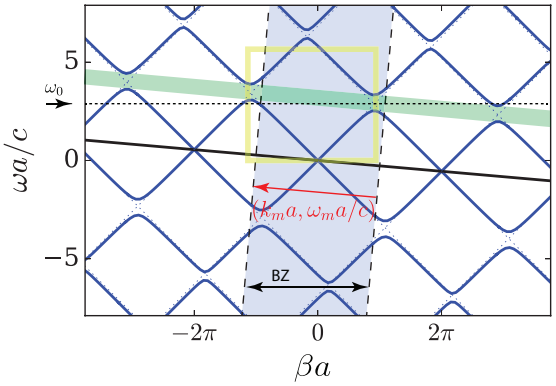


FIG. 2. Dispersion curves for an infinite space-time modulated medium with with permittivity (4). The solid curves correspond to modulation depth $M = 0.5$. The dotted lines represent the limit of vanishingly small modulation depth $M \to 0$. The red vector $(k_\mathrm{m}a, \omega_\mathrm{m}a/c)$ corresponds to the space-time modulation wavenumber and frequency, where $a = 2\pi/k_\mathrm{m}$ is the spatial period. The dashed lines represent the Brillouine zone. The highlighted green region represents the oblique bandgaps. The yellow window corresponds to the asymmetric bandgap structure in Fig. 1(b).

In the following, we assume the space-time profile or the periodic function $f$ has a sinusoidal form. In such a case, closed-form solutions can be derived for the determinant and corresponding eigenvectors. An example of dispersion curves for a space-time medium with permittivity

$$\epsilon(\mathbf{r}, t) = \epsilon_0 \epsilon_r \left[1 + M \cos\left(\omega_\mathrm{m} t - k_\mathrm{m} z\right)\right] \tag{4}$$

are plotted in Fig. 2. The solid curves correspond to modulation depth $M = 0.5$. The dotted lines to the limit of vanishingly small modulation depth $M \to 0$. The red vector $(k_\mathrm{m}a, \omega_\mathrm{m}a/c)$ corresponds to the space-time modulation wavenumber and frequency, where $a = 2\pi/k_\mathrm{m}$ is the spatial period.

Given any solution $(\beta, \omega)$ to dispersion equations, it can be easily shown that $(\beta \pm nk_\mathrm{m}, \omega \pm n\omega_\mathrm{m})$ represents an infinite set of solutions corresponding to the same mode. Therefore the dispersion curves are periodic along the vector $(k_\mathrm{m}, \omega_\mathrm{m})$. As a result the Brillouine zone, represented by the dashed lines in Fig. 2, is tilted. Therefore, in contrast to a spatial Bragg dispersion, the bandgaps appear asymmetric with respect to positive $(\beta > 0)$ and negative $(\beta < 0)$ directions of propagation, represented with the oblique green highlighted region in Fig. 2. The yellow window corresponds to the required asymmetric dispersion curve in Fig. 1(b). This asymmetry is leveraged in the following sections to generate space-time engineered optical isolation. However, accurate analysis of the structure requires taking all the dispersion diagram, including the regions outside the yellow window, into account. In the next sections, we develop an accurate full-wave modeling technique to calculate the scattering parameters for a space-time modulated slab. The proposed method identifies all the excited modes inside the slab and provides physical insight into the scattering mechanism.

## IV. SPACE-TIME MODULATED SLAB

The asymmetric bandgaps in the dispersion curves of a space-time-modulated slab may be leveraged for realizing optical isolation based on the principles explained in Sec. II. Consider the periodic space-time modulation (1) over a finite section of a background medium with permittivity $\epsilon_r$, as shown in Fig. 3. This structure may be analyzed with full-wave simulation techniques that can handle space-time varying media, such as the finite difference time domain (FDTD) method [51]. However, such an analysis does not provide much insight into the operation mechanism. To gain some physical insight we shall use the mode-matching analysis technique. In this techniques the excited Bloch-Floquet modes inside the slab, are clearly identified. In the mode-matching technique the electromagnetic field in the transmitted, reflected as well as the forward and backward propagating fields inside the slab are represented as a superposition of all the possible modal solutions in each region with unknown coefficients. With application of appropriate boundary conditions, the unknown coefficients corresponding to weighting factor of each mode is determined. Details are provided in the next sections.

### A. Mode-matching analysis

Consider an incident plane wave $\mathbf{E}^\mathrm{i} = \hat{\mathbf{x}} e^{j(\omega t - kz)}$ on a space-time modulated slab sandwitched between media with permittivity $\epsilon_r$, as shown in Fig. 3, where $k = \omega\sqrt{\epsilon_r}/c$. This incident wave will excite all the Bloch-Floquet modes inside the slab that include the incident frequency in their infinite set of space-time harmonics. These modes are represented in Fig. 4(a) with the red/yellow dots where the horizontal line representing the incident frequency crosses the dispersion curves. We decompose this set of modes into modes with positive group

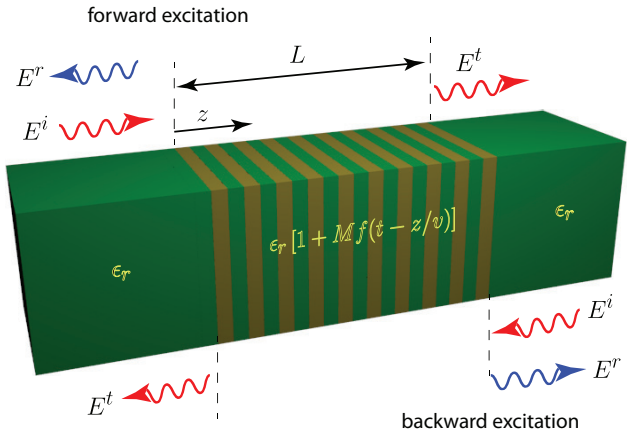


FIG. 3. Scattering from a space-time modulated slab. A finite part of a material with permittivity $\epsilon_r$ is modulated spatio-temporally with the space-time varying permittivity (1). The structure responds differently when excited from the left side or the right side, and is therefore nonreciprocal. Top arrows represent forward excitation, where the structure is excited from left. Bottom arrows represent backward excitation, i.e. the structure is excited from right.

velocity, or positive Poynting vector, represented by red dots, and expressed by the sum

$$\mathbf{E}^+(z,t) = \sum_{p=-\infty}^{\infty} a_p^+ \mathbf{E}_p^+(z,t), \tag{5}$$

and modes with negative group velocity, or negative Poynting vector, represented with yellow dots and expressed by the following sum

$$\mathbf{E}^-(z,t) = \sum_{p=-\infty}^{\infty} a_p^- \mathbf{E}_p^-(z,t). \tag{6}$$

In (5) and (6) $a_p^{\pm}$ represent the unknown coefficients, and each mode has the following Bloch-Floquet expression

$$\mathbf{E}_p^{\pm}(z,t) = \hat{\mathbf{x}} e^{j\left(\omega t - \beta_p^{\pm} z\right)} \sum_{n=-\infty}^{\infty} E_{p,n}^{\pm} e^{jn(\omega_\mathrm{m} t - k_\mathrm{m} z)}, \tag{7}$$

where $\beta_p$ represents the Bloch-Floquet wavenumber for the corresponding mode, i.e. the projection of the dots onto the horizontal axis. Our convention for numbering positive (red) and negative (yellow) propagating modes is apparent in Fig. 4(a), with the red/yellow number corresponding to red/yellow modes. Each of these red/yellow numbers correspond to the index $p$ in (5)/(6). Note that in a space-time modulated media all these excited modes are distinct, which can be verified by transferring them into the Brillouine zone, between the oblique dashed lines, as shown in Fig. 4(b). To find equivalent Bloch-Floquet modes, the modes outside the Brillouine zone are shifted by multiple integers of the vector $(k_\mathrm{m}a, \omega_\mathrm{m}a/c)$ until they reside in the Brillouine zone. In a conventional static Bragg structure, all the red/yellow points will fold back on the same red/yellow point in the Brillouine zone, i.e. are identical modes (linearly dependent), and therefore all but one must be discarded. However, in a space-time modulated medium, the numbered modes in Fig. 4(a) are distinct (linearly independent), and they should all be taken into account.

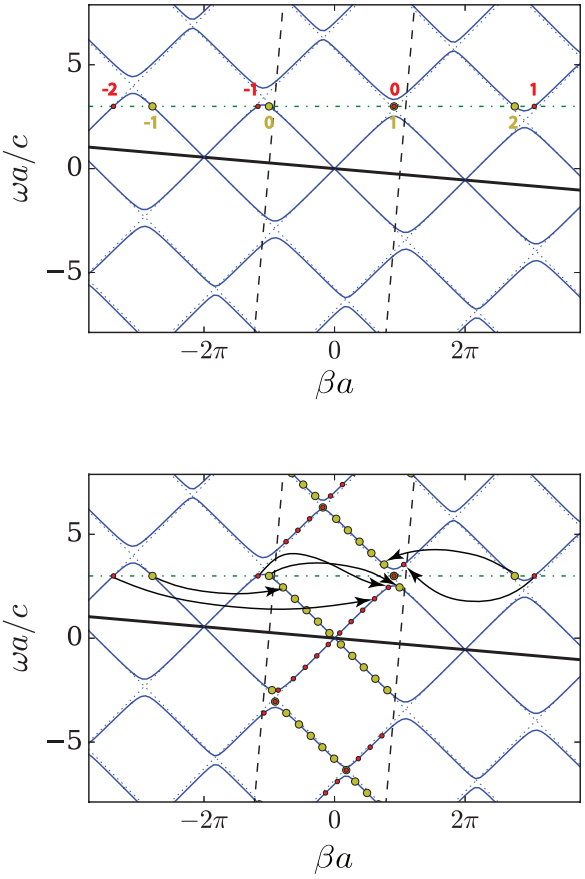


FIG. 4. Bloch-Floquet modes excited inside the space-time modulated slab. The horizontal dashed line represents the incident frequency and the dots represent the excited modes. Red dots represent the modes with a positive group velocity or positive Poynting power. Yellow dots represent the excited modes with negative group velocity or negative Poynting power. (b) The excited modes are transferred inside the Brillouine zone.

Reflected and transmitted waves are represented as superpositions of plane waves in a uniform medium with relative permittivity $\epsilon_r$ propagating in the $-z$ and $+z$ directions, respectively. Note that in order to satisfy the boundary conditions, the reflected and transmitted waves must include all the temporal frequencies excited inside the slab, i.e. $\omega + p\omega_\mathrm{m}$, $p = -\infty \cdots \infty$, i.e.

$$\mathbf{E}^{\mathrm{r}}(z,t) = \hat{\mathbf{x}} \sum_{p=-\infty}^{\infty} a_p^{\mathrm{r}} e^{j(\omega_p t + k_p z)}, \tag{8}$$

$$\mathbf{E}^{\mathrm{t}}(z,t) = \hat{\mathbf{x}} \sum_{p=-\infty}^{\infty} a_p^{\mathrm{t}} e^{j(\omega_p t - k_p z)}, \tag{9}$$

where $\omega_p = \omega + p\omega_{\mathrm{m}}$, $k_p = \omega_p\sqrt{\epsilon_r}/c$ and $a_p^{\mathrm{r}}$, $a_p^{\mathrm{t}}$ are unknown coefficients.

The magnetic field corresponding to each excited slab mode $\mathbf{E}_p^{\pm}$ in (7) follows from the Maxwell-Faraday equation $\nabla \times \mathbf{E} = -\mu_0 \frac{\partial}{\partial t}\mathbf{H}$, leading to

$$\mathbf{H}_p^{\pm}(z,t) = \hat{\mathbf{y}} e^{j\left(\omega t - \beta_p^{\pm} z\right)} \sum_{n=-\infty}^{\infty} H_{p,n}^{\pm} e^{jn(\omega_{\mathrm{m}} t - k_{\mathrm{m}} z)} \tag{10}$$

where

$$H_{p,n}^{\pm} = \frac{\beta_p^{\pm} + nk_{\mathrm{m}}}{\mu_0(\omega + n\omega_{\mathrm{m}})} E_{p,n}^{\pm}. \tag{11}$$

Application of the boundary conditions, i.e. continuity of the tangential electric and magnetic fields at the slab interfaces, then leads to a system of equations for the unknown coefficients, whose solutions provides the reflected and transmitted fields and the excited fields inside the slab.

### B. Results

Consider a space-time modulated slab with dispersion curves shown in Fig. 4(a), where the modulation frequency is tuned such that the incident frequency excites the gap mode (red index 0) in the forward direction, and a propagating mode (yellow index 0) in the backward direction, as shown in Fig. 4(a). As explained in the previous section, due to the tilted nature of the space-time diagrams, an infinite number of slab modes are excited. The operation of the device depends on the relative excitation strength of these modes. When the structure is excited from left/right, these slab modes are excited with different weighting factors, i.e. the structure exhibits nonreciprocity. In this section, reflection and transmission, as well as the excited modes inside the slab for excitation from left/right and the corresponding isolation are quantified.

#### 1. *Excitation from left*

Consider a space-time modulated slab with space-time permittivity (4), background permittivity $\epsilon_r = 12.25$, modulation depth $M = 0.02$, temporal and spatial modulation frequencies $\omega_{\mathrm{m}} = 0.13\omega_0$ and $k_{\mathrm{m}} = -2.27k_0$, respectively, and length $L = 200\lambda$, excited at the frequency $\omega_0 = 0.259c/a$, where $a$ is the spatial period of the space-time varying slab. This space-time permittivity profile represents a sinusoidal Bragg grating, whose permittivity profile is shifted to the left inside the space-time modu-

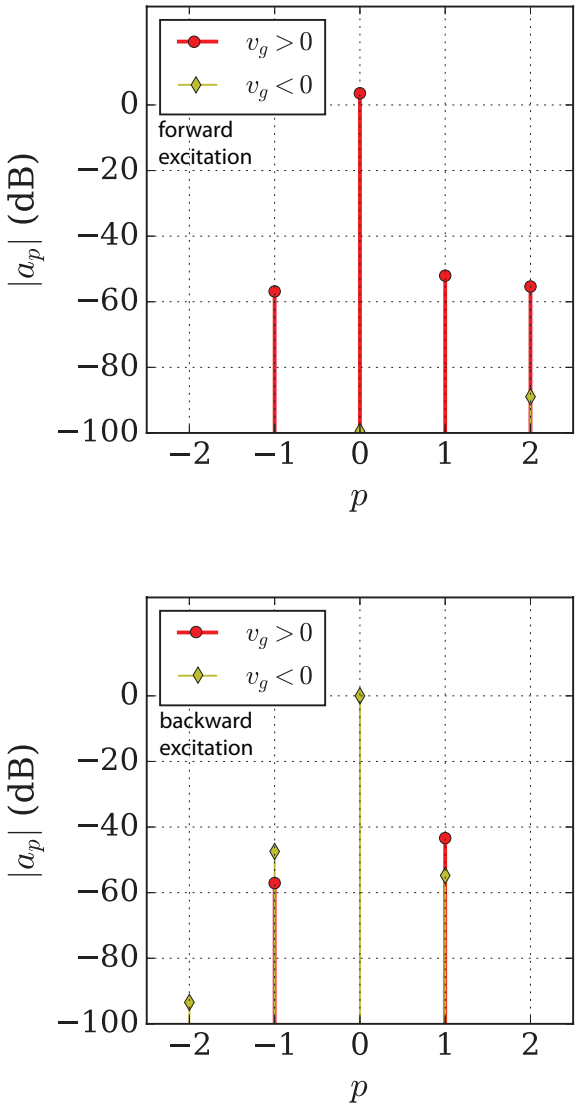


FIG. 5. Magnitude of the excited modes inside a space-time modulated slab with space-time permittivity (4), background permittivity $\epsilon_r = 12.25$, modulation depth $M = 0.02$, temporal and spatial modulation frequencies $\omega_{\mathrm{m}}/\omega_0 = 0.13$, $k_{\mathrm{m}}/k_0 = -2.27$ and length $L = 200\lambda$. (a) The slab is excited from the left side. The gap mode (red index 0 in Fig. 4(a)) is excited dominantly. All the other forward propagating modes (red) and backward propagating modes (yellow) are excited very weakly. (b) The slab is excited from the right side. The dominantly excited mode is a propagating mode (yellow index 0 in Fig. 4(a)).

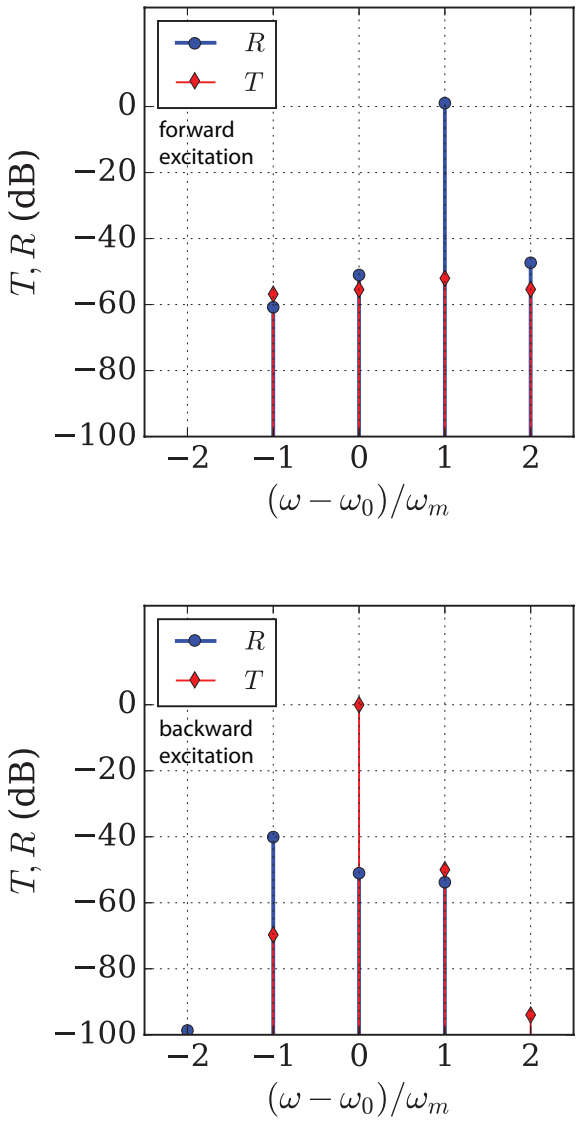


FIG. 6. Reflection and transmission in dB for a space-time modulated slab with the same parameters as in Fig. 6. (a) The slab is excited from the left side. The dominantly excited evanescent gap mode decays exponentially and conveys no power to the transmitted region. All of the power is reflected. The reflected wave is red-shifted. (b) The slab is excited from the right side. The dominantly excited propagating mode transfers all its energy to the other end. Almost all the power is transmitted at the fundamental frequency $\omega_0$.

lated region, with velocity $\omega_{\rm m}/k_{\rm m}$. For excitation from the left side, the amplitude of the excited modes inside the slab, calculated by the mode-matching analysis presented in the previous section, are presented in Fig. 5(a). The red lines/dots correspond to positive group velocity (forward propagating) Bloch-Floquet modes, while the yellow lines/dots correspond to negative group velocity (backward propagating) modes. The mode falling in the bandgap is the one with the strongest excitation level. This mode has the closest Bloch-Floquet wavenumber to the wavenumber of the incident wave. We will show in the next section that this result is closely related to the impedance and the specific electromagnetic profile of this mode. All the other modes are only very weakly excited, at least 50 dB below the gap mode. Therefore, all the modes falling outside the highlighted yellow window in Fig. 4(a) play an insignificant role, and the performance of the space-time modulated slab can be closely predicted by the intuitive picture presented in Fig. 1(b).

As the dominantly excited slab mode is evanescent, it decays exponentially and conveys almost no power to the other end. Therefore the structure is highly reflective. The reflected amplitudes for different frequencies are plotted in Fig. 6(a). The transmitted power can be controlled by tuning the modulation depth and the length of the slab. For any modulation depth, it is possible to reduce the transmitted power to the desired level by increasing the length of the slab. Also notice that the reflected power is slightly greater than unity, which is not violating energy conservation since in a space-time varying medium energy is pumped into the system and total energy is not conserved. In contrast to what would happen in a static Bragg grating, the wave reflected from the space-time slab is shifted in term s of temporal frequency, specifically blue-shifted. This blue-shift resembles a Doppler shift, as the space-time varying medium profile has a negative phase velocity $v_{\rm m} = \omega_{\rm m}/k_{\rm m}$ with respect to a source on the left. This frequency shift is exactly equal to the modulation frequency of the space-time medium. This frequency shift corresponds neither to the conventional relativistic Doppler shift for a reflected wave from a moving object with velocity $v_{\rm m}$ given by

$$\Delta\omega = \left(\frac{1+v_{\rm m}/c}{1-v_{\rm m}/c} - 1\right)\omega_0, \tag{12}$$

nor to its classical limit $v_{\rm m} \ll c$

$$\Delta\omega = 2\frac{v_{\rm m}}{c}\omega_0. \tag{13}$$

This anomalous Doppler shift is explained in Sec. IV B 3.

### 2. *Excitation from right*

For excitation from the right side, the amplitude of the modes excited inside the slab are presented in Fig. 5(b). The red lines/dots correspond to positive group velocity (forward propagating) Bloch-Floquet modes, while the yellow lines/dots correspond to negative group velocity (backward propagating) modes. The negative group velocity (backward propagating) mode with yellow index 0 is excited predominantly. This mode has the Bloch-Floquet wavenumber that is the closest to the wavenumber of the incident wave and is thus almost perfectly matched to the incident wave. As this slab mode is a

propagating mode, it conveys almost all the power to the other end. Therefore the structure is highly transparent. The transmitted and reflected harmonics are plotted in Fig. 6(b). The level of the reflected power is proportional to the modulation depth. For a modulation depth $M = 0.02$, the reflected power is less than $-40$ dB.

### 3. *Explanation of the frequency up-shift in the reflected wave*

Although the boundaries of the space-time modulated slab considered in Fig. 3 are static, the space-time profile (4) is moving to left/right with phase velocity $v_\mathrm{m} = \omega_\mathrm{m}/k_\mathrm{m}$. The reflected wave from the bandgap structure exhibits a frequency shift whose sign resembles a Doppler shift. However, as discussed in Sec. IV B 1, the value of the phase shift, which exactly equals the modulation frequency $\omega_\mathrm{m}$, does not correspond to a conventional Doppler effect.

This frequency shift can be explained based on interband photonic transitions between forward propagating and backward propagating modes of a single-mode waveguide. For small modulation depths $M \ll 1$, instead of considering the exact periodic problem involving infinite space-time harmonics, the problem may be approximated as follows. As an electromagnetic wave with momentum and frequency $(k_0, \omega_0)$ in the background medium enters the space-time modulated section (4), the space-time medium will provide momentum and energy corresponding to $\pm(k_\mathrm{m}, \omega_\mathrm{m})$ to the wave. If the shift in the momentum and energy $(k_0 \pm k_\mathrm{m}, \omega_0 \pm \omega_\mathrm{m})$ corresponds to a mode of the waveguide, it can be shown based on a coupled-mode analysis that the incoming waveguide mode is gradually transformed to the waveguide mode at $(k_0 \pm k_\mathrm{m}, \omega_0 \pm \omega_\mathrm{m})$. However, if $(k_0 \pm k_\mathrm{m}, \omega_0 \pm \omega_\mathrm{m})$ does not correspond to a mode of the waveguide, it passes through the space-time modulated region almost unaffected. This interband transition picture and the associated coupled mode analysis are accurate only for very small modulation depths, and should be avoided for strong modulations, as they ignore the rich spectral features of the electromagnetic band structure in a space-time modulated system. Nonetheless, they provide an intuitive picture of the frequency shift observed in the previous section.

For the space-time modulated problem considered in the previous section, the dispersion curves of the single mode background medium and the corresponding momentum and energy $\pm(k_\mathrm{m}, \omega_\mathrm{m})$ provided by the space-time medium are plotted in Fig. 7(a), when the slab is excited from the left. As $(k_0 + k_\mathrm{m}, \omega_0 + \omega_\mathrm{m})$ corresponds to a backward propagating mode of the waveguide, the forward propagating mode gradually transforms to a blue-shifted backward propagating mode, i.e. reflects with a frequency up-shift exactly equal to $\Delta\omega = \omega_\mathrm{m}$.

For a wave exciting the space-time modulated region from the right side, the corresponding momentum and energy $\pm(k_\mathrm{m}, \omega_\mathrm{m})$ provided by the space-time medium is plotted in Fig. 7(b). As $(k_0 + k_\mathrm{m}, \omega_0 + \omega_\mathrm{m})$ does not correspond to a waveguide mode, it passes through the space-time region almost unaffected.

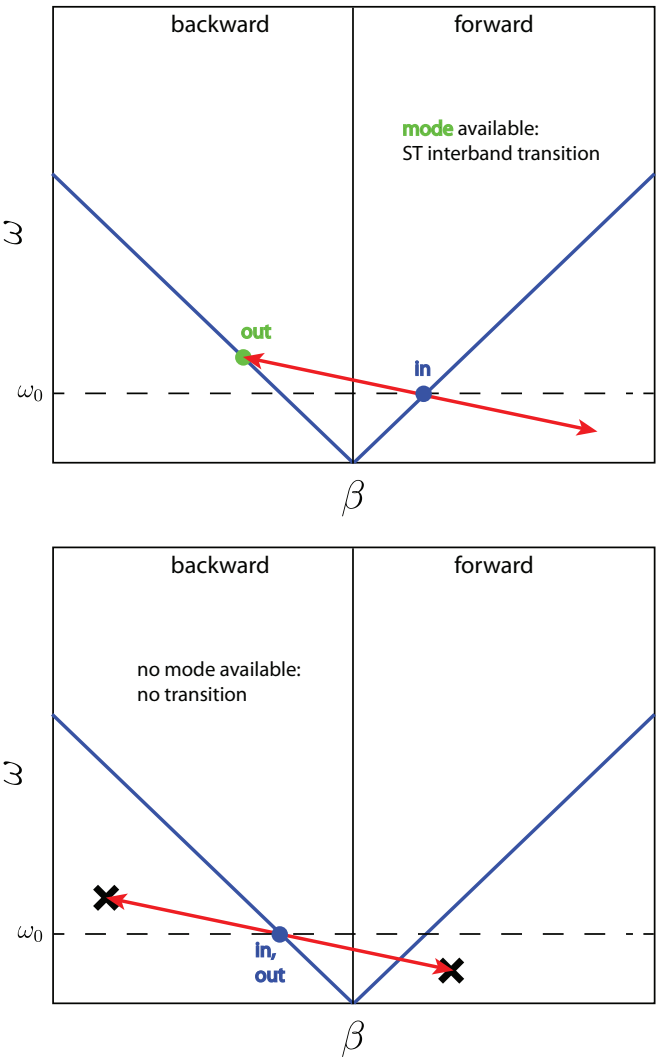


FIG. 7. Explanation of the frequency up-shift in the reflected field based on interband photonic transitions. The red arrows represent the momentum end energy provided by the space-time modulated region $\pm(k_\mathrm{m}, \omega_\mathrm{m})$ (a) Forward excitation: the forward propagating mode gradually transforms into a backward propagating mode with frequency $\omega_0 + \omega_\mathrm{m}$ and is reflected. (b) The backward propagating mode passes through the space-time section as $(k_0 \pm k_\mathrm{m}, \omega_0 \pm \omega_\mathrm{m})$ does not correspond to any waveguide mode.

To see how the forward propagating wave is transformed into a backward propagating wave at an up-shifted frequency when the structure is excited from the left, it is instructive to inspect the electric and magnetic field profiles of the dominantly excited gap mode. The electric field profile for the gap mode (red index 0 in Fig. 4(a)) and its corresponding temporal frequency spectrum are plotted in Fig. 8(a) and Fig. 8(b), respectively. This evanescent mode has two dominant frequency har-

monics at $\omega_0$ and $\omega_0 + \omega_m$, where $\omega_0$ is the incident frequency and $\omega_m$ is the modulation frequency. The rest of the frequency harmonics are at least 50dB weaker, and may be safely ignored. The ratio of the electric to the magnetic field for each harmonic, i.e. its effective refractive index, normalized to the refractive of the incident region, i.e. $n_0 = 1/\sqrt{\epsilon_r}$ is plotted in Fig. 9.

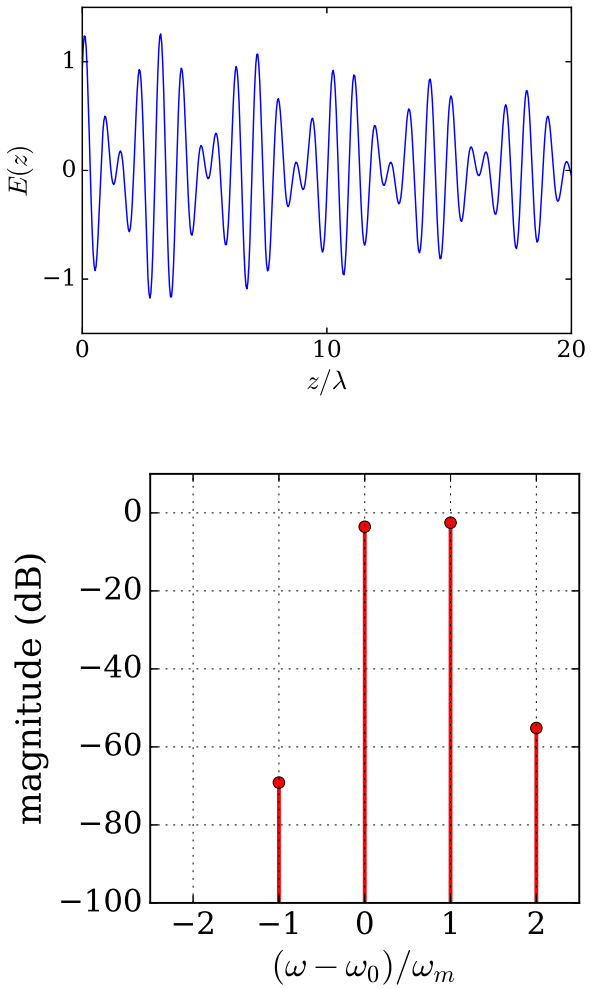


FIG. 8. Electric field pattern and frequency spectrum of the gap mode. (a) The electric field pattern for the evanescent gap mode, corresponding to red index 0 in Fig. 4(a). (b) Frequency harmonics of the evanescent gap mode plotted in (a). This mode has only two significant harmonics at frequencies $\omega_0$ and $\omega_0 + \omega_m$.

The harmonic at the fundamental frequency $\omega_0$ is forward propagating, $n_\omega > 0$, and completely matched to the incident medium i.e. $n_\omega = n_0$. The harmonic at frequency $\omega_0 + \omega_m$ has a negative effective refractive index $n_{\omega+\omega_m} = -n_0$. Therefore this harmonic is propagating backward and also fully matched to the incident medium. The red-shift mechanism is explained schematically in Fig. 10. As the incident wave and the forward harmonic are fully matched and have the same frequency $\omega_0$, the

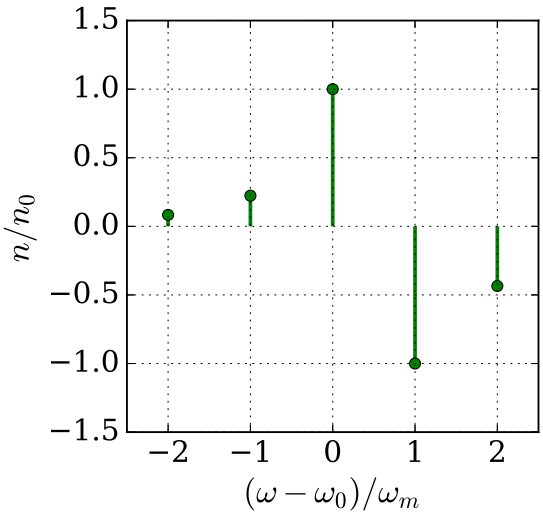


FIG. 9. Effective refractive index for different harmonics of the gap mode plotted in Fig. 8. Each point represents the effective refractive index corresponding to the ratio $E_n/H_n$ for the frequency harmonic $\omega_n = \omega_0 + n\omega_m$. The harmonic at frequency $\omega_0$ has a positive refractive index (forward propagating), and is fully matched to the incident region. The harmonic at frequency $\omega_0 + \omega_m$ has a negative refractive index (backward propagating), and is fully matched to the incident region.

incident signal excites this harmonic without any reflection at frequency $\omega_0$. The forward harmonic is evanescent and exponentially decays inside the slab. As it decays it is converted to the backward propagating harmonic, which exponentially grows towards the interface with frequency $\omega_0 + \omega_m$. This effect is clearly seen in the time domain simulation of the gap mode (see supplemental material [52]). The backward harmonic, which is also fully matched to the incident region, then excites the reflected wave at frequency $\omega_0 + \omega_m$ when it hits the interface, without any back-reflection inside the slab.

## V. DISCUSSION

Breaking Lorentz reciprocity using space-time engineered asymmetric photonic bandgaps, eliminates the bulky magnet in conventional nonreciprocal devices and is compatible with silicon photonics and integrated optoelectronics. The proposed method can achieve very high isolation levels irrespective of the modulation strength. For a given modulation depth, by properly controlling the length of the space-time modulated region, the desired isolation levels may be achieved. Isolation levels for different modulation depths and slab lengths are plotted in Fig. 11. As the modulation becomes weaker longer space-time sections are required to get the desired isolation levels. Note that for each modulation depth, isolation saturates at a specific level as the length of the

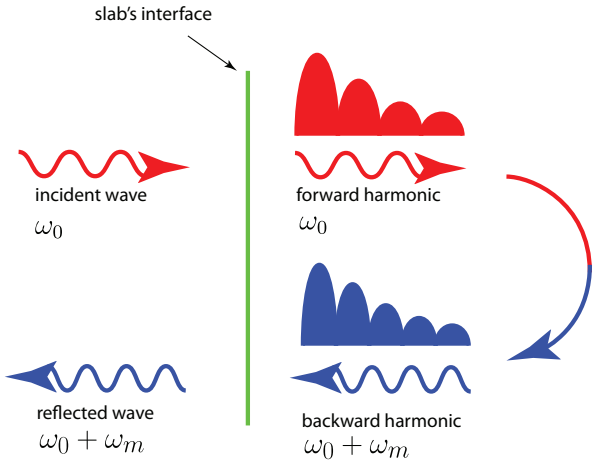


FIG. 10. Transformation of an incident forward propagating wave to an up-shifted backward propagating wave. An incident field with frequency $\omega_0$ impinges on the slab from the left side. The only 2 significant harmonics of the gap mode at frequencies $\omega_0$ and $\omega_0 + \omega_m$ are represented at the right side, where $\omega_m$ is the modulation frequency. The incident wave is fully matched to the evanescent harmonic at frequency $\omega_0$, therefore it excites this harmonic without back-reflection. The excited evanescent harmonic at frequency $\omega_0$ decays exponentially inside the slab, and its energy is transferred to the backward propagating harmonic at frequency $\omega_0 + \omega_m$, whose energy increases exponentially as it reaches the slab interface. The backward propagating harmonic is fully matched to the incident region. It excites the reflected wave at frequency $\omega_0 + \omega_m$ without any back-reflection inside the slab.

space-time modulated section is increased. This saturation is caused by coupling to the undesirable propagating modes of the space-time slab (red indices -1, 1, -2, 2...). For weaker modulations, coupling to these undesirable propagating modes is weaker, and therefore higher isolation levels are achievable.

The required modulation frequency for creating the necessary asymmetric bandgaps is relatively low. The required modulation frequency is proportional to the width of the bandgap, which is directly proportional to the modulation depth. For lower modulation levels the bandgaps are narrower, therefore it takes a smaller modulation frequency to misalign the forward and backward gaps. For very small modulation depths $M \ll 1$ the width of the first bandgap can be approximated as $\Delta\omega/\omega_0 = 2M/[\pi(1-M)]$ [53]. Therefore, a modulation frequency $\omega_m = \Delta\omega = 2M/[\pi(1-M)]$ is sufficient to displace the bandgaps for nonreciprocal behavior. By decreasing the modulation depth, the modulation frequency can be decreased as much as desired. For modulation depths smaller than $10^{-7}$ optical isolation may be achieved through ultrasound waves. However, isolation bandwidth would be proportionally small, and the length of the device would be proportionally long. In such cases, wrapping the waveguide in the form of a space-time modulated coupled ring resonator, normally reduces the

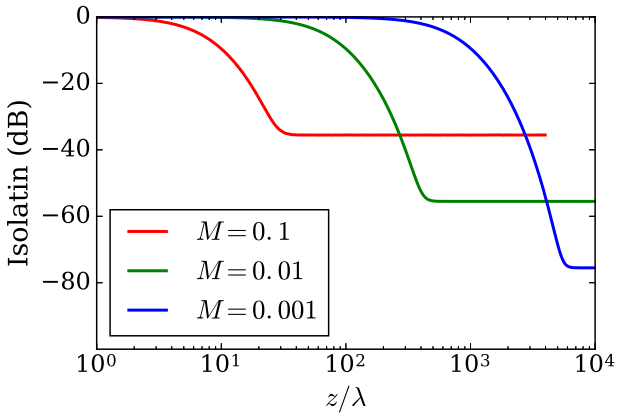


FIG. 11. Isolation per length for different modulation depths. For weaker modulations, longer space-time sections are required to get a specific amount of isolation. For each modulation depth, the corresponding isolation saturates at a specific level. This saturation is due to coupling to undesired propagating modes. For weaker modulations, coupling to undesired modes is weaker and higher isolation levels are achievable.

device footprint dramatically.

The bandwidth of unidirectional operation is directly proportional to the width of the bandgap. For smaller modulation depths, the corresponding isolation bandwidth gets narrowed. For different modulation depths, the corresponding isolation is plotted in Fig. 12. The lengths of the space-time slabs are chosen according to the saturation isolation in Fig. 11. For modulation depths $M = 0.1$, $M = 0.01$ and $M = 0.001$, the corresponding bandwidth is less than 5%, 1% and 0.1%, respectively. A given bandwidth and isolation level may be produced by an interplay between the modulation depth, and the length of the space-time modulated section.

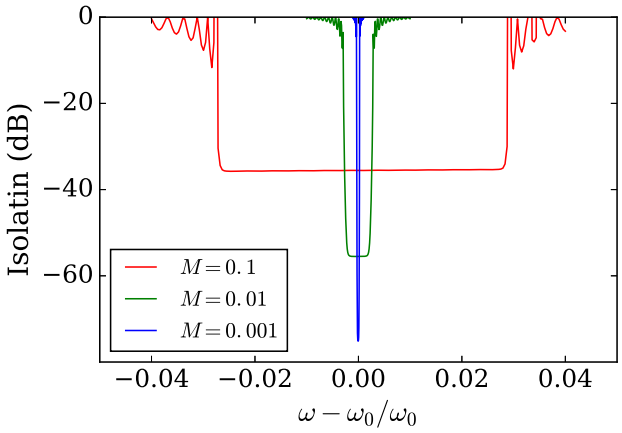


FIG. 12. Isolation bandwidth for different modulation depths. Bandwidth is directly proportional to modulation depth. For each modulation depth, the length of the space-time slab is chosen based on the saturation isolation in Fig. 11.

It should be noted that asymmetric photonic bandgaps can be produced in moving photonic crystals as well [54]. In the reference frame of a moving photonic crystal, co-propagating waves are red-shifted, and counter-propagating waves are blue-shifted. Wang et al. [54] uses this asymmetric Doppler shift for realization of optical diodes. The moving photonic crystal is emulated by an electromagnetically induced transparency (EIT) medium [55–57] controlled via a moving laser field pattern. However, it should be noted that although moving media and space-time modulated systems produce qualitatively similar results, the resulting effects have completely different nature. The frequency shift of the bandgaps in a moving photonic crystal is a direct consequence of the relativistic Doppler effect and equal to the relativistic Doppler shift. However, in a space-time varying medium the frequency shift of the bandgaps is a consequence of the space-time periodicity of the system, and the corresponding frequency shift in the reflected field is a consequence of the interband photonic transitions as explained in Sec. IV B 3. Moreover, in the reference frame of an static observer, a moving photonic crystal exhibits bianisotropic material properties and should be modeled accordingly [58–60]. Using Lorentz transformation, a moving photonic crystal can be modeled as a static photonic crystal by transforming to the reference frame of the moving photonic crystal. However, there is no general transformation that can reduce a space-time varying medium to a static problem.

Finally, as the forward excited wave is fully reflected at a shifted frequency, the structure can operate as an efficient optical mixer. The incident signal is up-shifted if the structure is excited from left at the forward bandgap tilted downwards, and it is down-shifted when the structure is excited from right at the backward bandgap tilted upward as shown in Fig. 13. The amount of frequency shift is directly controlled by the modulation frequency. The structure exhibits perfect mixing as the incident power is almost fully transferred to the desired up- or down-shifted frequency, without generating any undesirable harmonic and inter-modulation products.

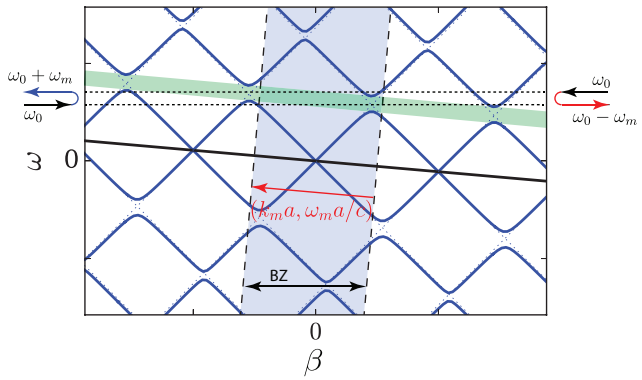


FIG. 13. Operation of a space-time engineered mixer based on asymmetric photonic bandgaps. When the structure is excited from left at the down-tilted forward bandgap the wave is fully reflected and up-shifted. When the structure is excited from right at the up-tilted backward bandgap the wave is fully reflected and down-shifted.

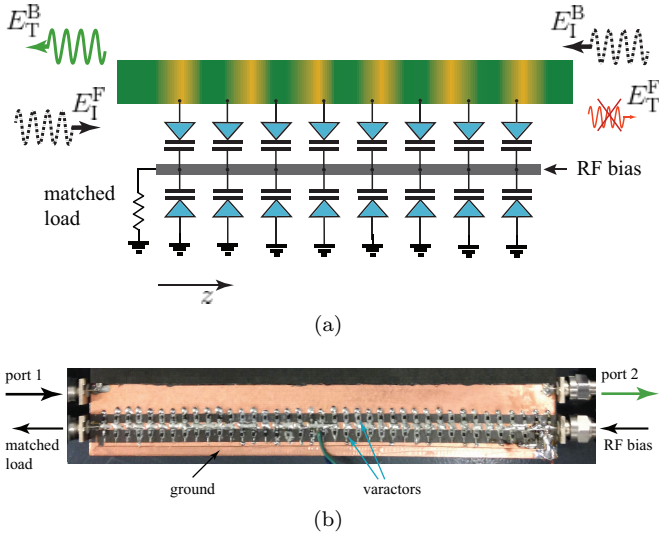


FIG. 14. Experimental realization of the space-time varying medium (4) at microwave. (a) Schematic of the space-time varying transmission line. The parameters of the microstrip lines are modified spatio-temporally through voltage controlled varactors. (b) The photograph of the realized space-time varying microstrip circuit.

## VI. EXPERIMENTAL DEMONSTRATION

The space-time varying medium (4) was realized at microwave frequencies using the space-time varying microstrip transmission line shown in Fig. 14. The transmission line is loaded with an array of sub-wavelengthly spaced shunt varactors. The bias line in the middle provides a DC bias $V_{\rm DC}$ as well as a propagating RF bias for the varactors, i.e. the voltage across the varactors is

$$V(z,t) = V_{\rm DC} + V_{\rm m}\cos(\omega_{\rm m}t + k_{\rm m}z), \qquad (14)$$

where $\omega_{\rm m}$ is the modulation frequency. The bias phase velocity $v_{\rm m} = \omega_{\rm m}/k_{\rm m}$ is dictated by the bias line capacitance ($C_{\rm m}$) and inductance ($L_{\rm m}$), i.e. $v_{\rm m} = 1/\sqrt{L_{\rm m}C_{\rm m}}$. The varactors in the reverse biased by the bias line and act as voltage controlled capacitors. Therefore, the varactors provide a space-time varying capacitance

$$C(z,t) = C_{\rm av} + C_{\rm m}\ \cos(\omega_{\rm m}t + k_{\rm m}z) \qquad (15)$$

to the signal transmission line. The structure in Fig. 14 therefore emulates a material with time varying permittivity as in (4), with $\epsilon_r = C_{\rm av}$ and $M = C_{\rm m}/C_{\rm av}$.

Figure 14 shows a photograph of the space-time varying microstrip line. The modulation parameters are

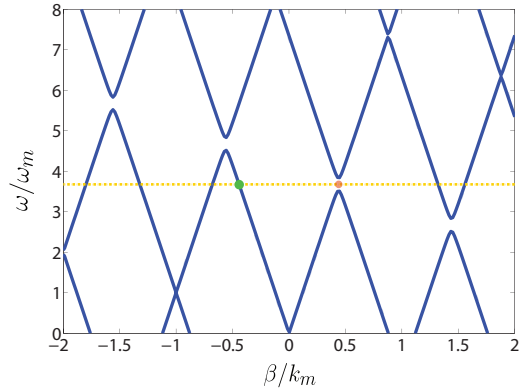


FIG. 15. Dispersion curve corresponding to the space-time varying transmission line in with parameters $\omega_\mathrm{m} = 2\pi \times 0.675$ GHz, $k_\mathrm{m} = 415.79$ rad/m and $M = C_\mathrm{m}/C_\mathrm{av} = 0.15$

$\omega_\mathrm{m} = 2\pi \times 0.675$ GHz, $k_\mathrm{m} = 415.79$ rad/m and $M = C_\mathrm{m}/C_\mathrm{av} = 0.15$. The modulation circuit is comprised of 39 unit cells of antiparallel varactors, uniformly distributed along the microstrip line, with the subwavelength period $p = 5$ mm, corresponding to $p/\lambda_\mathrm{m} \approx 1/19$. Therefore, the structure safely represents a medium with continuous permittivity (4). The varactors were the BB833 model from Infineon Technologies with capacitance ratio, $C_\mathrm{max}/C_\mathrm{min} = 12$. The structure has length $L = 8$ in and is excited at $\omega_0 = 2\pi \times 2.5$ GHz. The substrate is RT6010 with permittivity $\epsilon_\mathrm{r} = 10.2$, thickness $h = 100$ mil and $\tan\delta = 0.0023$. The corresponding dispersion curves are plotted in Fig. 15, with the horizontal line representing the excitation frequency.

The scattering parameters are plotted in Fig. 16. As expected, in the forward direction the evanescent gap mode marked by the red dot in Fig. 15 is dominantly excited. This mode decays exponentially and carries little energy to the transmission side. For the realized structure in Fig. 14 the evanescent mode decays 10.5 dB before reaching the other end, corresponding to -10.5 dB transmission in Fig. 16(a). The rest of the power is reflected at the up-shifted frequency $\omega_0 + \omega_m$. In the backward direction the incident wave is dominantly coupled to the backward propagating mode marked by the green dot in Fig. 15 and is almost fully transmitted. The corresponding isolation level is 10.5 dB. Higher isolation levels may be achieved by increasing the length of the structure.

## VII. CONCLUSIONS

space-time modulation was used to tilt the band structure of photonic crystals, resulting in asymmetrically-aligned photonic bandgaps for opposite directions of propagation. Such space-time modulated slabs were excited at the frequency corresponding to a photonic bandgap, exciting the evanescent bandgap mode in the forward direction while exciting a propagating mode in the opposite direction. Using a full-wave modal analysis

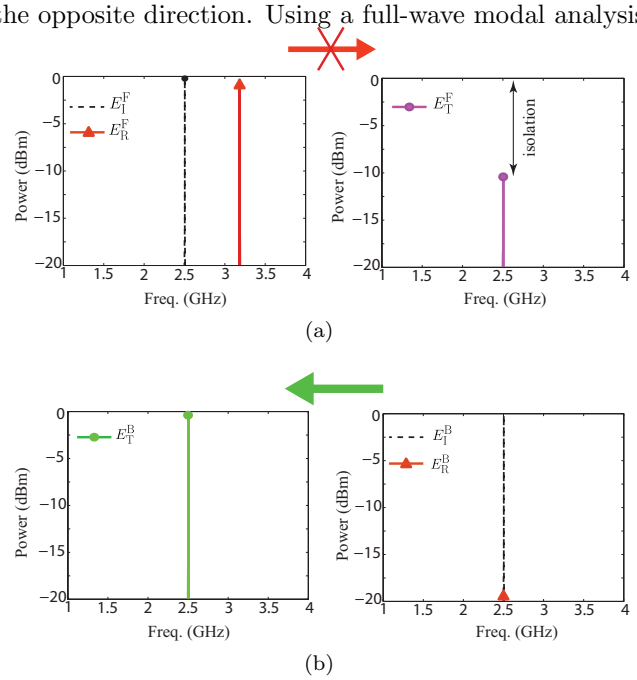


FIG. 16. Experimental results for the isolator in Fig. 14 for $\omega_0 = 2\pi \times 2.5$ GHz, $\omega_\mathrm{m} = 0.27\omega_0$, $k_\mathrm{m} = 2.27k_0$, $L = 6\lambda_0$ and $M = 0.15$. (a) Forward excitation. The wave is almost fully reflected at the blue-shifted frequency $\omega_\mathrm{refl} = \omega_0 + \omega_\mathrm{m} = 2\pi \times 3.175$ GHz. The dominantly excited evanescent gap mode decays exponentially and carries little energy to the other end (less than -10 dB). (b) Backward excitation. The backward incident wave is coupled dominantly to the backward propagating slab mode marked by the green dot in Fig. 15 at is fully transmitted at $\omega_0$. All the rest of the temporal harmonics $\omega_0 + n\omega_\mathrm{m}$ not shown, are weaker than $-19$ dBm.

it was shown that in the forward direction all the energy is reflected at a blue-shifted frequency, corresponding to an anomalous Doppler shift. In the opposite direction the incident wave is fully transferred to the other end of the space-time modulated slab by strongly coupling to one of its propagating modes, realizing an optical isolator. The proposed method may find applications as integrated photonic isolators and integrated perfect mixers.

[1] A. G. Gurevich and G. A. Melkov, *Magnetization oscillations and waves* (CRC press, 1996).

[2] B. E. Saleh, M. C. Teich, and B. E. Saleh, *Fundamentals of photonics*, Vol. 22 (Wiley New York, 1991).

[3] A. Hartstein and E. Burstein, Solid State Communications **14**, 1223 (1974).
[4] J. Montoya, K. Parameswaran, J. Hensley, M. Allen, and R. Ram, Journal of Applied Physics **106**, 023108 (2009).
[5] N. Chamanara, D. L. Sounas, T. Szkopek, and C. Caloz, Optics express **21**, 25356 (2013).
[6] N. Chamanara, D. L. Sounas, and C. Caloz, Optics express **21**, 11248 (2013).
[7] N. Chamanara and C. Caloz, Phys. Rev. B **94**, 075413 (2016).
[8] R. Soref, IEEE Journal of selected topics in quantum electronics **12**, 1678 (2006).
[9] L. Pavesi and D. J. Lockwood, *Silicon photonics*, Vol. 1 (Springer Science & Business Media, 2004).
[10] G. T. Reed and A. P. Knights, West Sussex, England: John Wiley and Sons, Ltd (2004).
[11] B. Jalali and S. Fathpour, Journal of lightwave technology **24**, 4600 (2006).
[12] S. Tanaka, N. Shimomura, and K. Ohtake, Proceedings of the IEEE **53**, 260 (1965).
[13] M. A. Smith, in *Microwave Symposium Digest, 1988., IEEE MTT-S International* (IEEE, 1988) pp. 1015–1016.
[14] Y. Ayasli, IEEE Transactions on Magnetics **25**, 3242 (1989).
[15] C. Kalialakis, M. J. Cryan, P. S. Hall, and P. Gardner, IEEE Transactions on Microwave Theory and Techniques **48**, 1017 (2000).
[16] T. Kodera, D. L. Sounas, and C. Caloz, Applied Physics Letters **99**, 031114 (2011).
[17] T. Kodera, D. L. Sounas, and C. Caloz, Microwave Theory and Techniques, IEEE Transactions on **61**, 1030 (2013).
[18] D. L. Sounas, T. Kodera, and C. Caloz, IEEE Transactions on Antennas and Propagation **61**, 221 (2013).
[19] Z. Wang, Z. Wang, J. Wang, B. Zhang, J. Huangfu, J. D. Joannopoulos, M. Solja00i04, and L. Rana, Proc. Nat. Acad. Sci. USA **109**, 13194C13197 (2012).
[20] S. Taravati, B. A. Khan, S. Gupta, K. Achouri, and C. Caloz, arXiv:1608.07324v2 [physics.class-ph] (2016).
[21] N. Reiskarimian and H. Krishnaswamy, Nature Communications **7** (2016).
[22] G. Carchon and B. Nanwelaers, IEEE Transactions on Microwave Theory and Techniques **48**, 316 (2000).
[23] B. Peng, S. K. Ozdemir, F. Lei, F. Monifi, M. Gianfreda, G. L. Long, S. Fan, F. Nori, C. M. Bender, and L. Yang, arXiv preprint arXiv:1308.4564 (2013).
[24] L. Fan, J. Wang, L. T. Varghese, H. Shen, B. Niu, Y. Xuan, A. M. Weiner, and M. Qi, Science **335**, 447 (2012).
[25] M. Soljačić, C. Luo, J. D. Joannopoulos, and S. Fan, Optics letters **28**, 637 (2003).
[26] K. Gallo, G. Assanto, K. R. Parameswaran, and M. M. Fejer, Applied Physics Letters **79**, 314 (2001).
[27] A. M. Mahmoud, A. R. Davoyan, and N. Engheta, Nature communications **6** (2015).
[28] M. D. Tocci, M. J. Bloemer, M. Scalora, J. P. Dowling, and C. M. Bowden, Applied physics letters **66**, 2324 (1995).
[29] Y. Shi, Z. Yu, and S. Fan, Nature photonics **9**, 388 (2015).
[30] C. E. Rüter, K. G. Makris, R. El-Ganainy, D. N. Christodoulides, M. Segev, and D. Kip, Nature Physics **6**, 192 (2010).
[31] Z. Lin, H. Ramezani, T. Eichelkraut, T. Kottos, H. Cao, and D. N. Christodoulides, Physical Review Letters **106**, 213901 (2011).
[32] U. Al Khawaja, S. Al-Marzoug, H. Bahlouli, and Y. S. Kivshar, Physical Review A **88**, 023830 (2013).
[33] B. Peng, S. K. Ozdemir, F. Lei, F. Monifi, M. Gianfreda, G. L. Long, S. Fan, F. Nori, C. M. Bender, and L. Yang, arXiv preprint arXiv:1308.4564 (2013).
[34] L. Chang, X. Jiang, S. Hua, C. Yang, J. Wen, L. Jiang, G. Li, G. Wang, and M. Xiao, Nature photonics **8**, 524 (2014).
[35] C. He, M.-H. Lu, X. Heng, L. Feng, and Y.-F. Chen, Physical Review B **83**, 075117 (2011).
[36] L. Feng, Y.-L. Xu, W. S. Fegadolli, M.-H. Lu, J. E. Oliveira, V. R. Almeida, Y.-F. Chen, and A. Scherer, Nature materials **12**, 108 (2013).
[37] K. G. Makris, R. El-Ganainy, D. N. Christodoulides, and Z. H. Musslimani, Physical Review A **81**, 063807 (2010).
[38] M. Kulishov, J. Laniel, N. Bélanger, J. Azaña, and D. Plant, Optics express **13**, 3068 (2005).
[39] L. Poladian, Physical Review E **54**, 2963 (1996).
[40] Z. Yu and S. Fan, Nature photonics **3**, 91 (2009).
[41] D. L. Sounas, C. Caloz, and A. Alu, Nature communications **4** (2013).
[42] N. A. Estep, D. L. Sounas, J. Soric, and A. Alù, Nature Physics **10**, 923 (2014).
[43] M. Hafezi and P. Rabl, Optics express **20**, 7672 (2012).
[44] S. Taravati and C. Caloz, IEEE Trans. on Antennas & Prop. (2017), to be published.
[45] A. Cullen, Nature **181** (1958).
[46] P. Tien, Journal of Applied Physics **29**, 1347 (1958).
[47] A. Oliner and A. Hessel, IRE Transactions on Antennas and Propagation **7**, 201 (1959).
[48] E. Cassedy and A. Oliner, Proceedings of the IEEE **51**, 1342 (1963).
[49] E. Cassedy, Proceedings of the IEEE **55**, 1154 (1967).
[50] R. Chu and T. Tamir, Electrical Engineers, Proceedings of the Institution of **119**, 797 (1972).
[51] A. Taflove and S. C. Hagness, *Computational electrodynamics* (Artech house publishers, 2000).
[52] See the supplemental materials at [URL] for electric field animations for the gap mode in Fig. 8.
[53] J. D. Joannopoulos, S. G. Johnson, J. N. Winn, and R. D. Meade, *Photonic crystals: molding the flow of light* (Princeton university press, 2011).
[54] D.-W. Wang, H.-T. Zhou, M.-J. Guo, J.-X. Zhang, J. Evers, and S.-Y. Zhu, Physical review letters **110**, 093901 (2013).
[55] K.-J. Boller, A. Imamoğlu, and S. E. Harris, Physical Review Letters **66**, 2593 (1991).
[56] S. Harris, J. Field, and A. Imamoğlu, Physical Review Letters **64**, 1107 (1990).
[57] M. Fleischhauer, A. Imamoglu, and J. P. Marangos, Reviews of modern physics **77**, 633 (2005).
[58] J. Plebanski, Physical Review **118**, 1396 (1960).
[59] R. T. Thompson, S. A. Cummer, and J. Frauendiener, Journal of Optics **13**, 024008 (2010).
[60] S. A. Tretyakov, I. S. Nefedov, and P. Alitalo, New Journal of Physics **10**, 115028 (2008).